Submitted to the 30th International Conference on High-Energy Physics ICHEP2000,
Osaka, Japan, July 2000

Dijet Production in Charged and Neutral Current e^+p Interactions at high Q^2

H1 Collaboration

Abstract

Jet production in charged and neutral current events in the kinematic range of Q^2 from 640 to 35 000 GeV^2 is studied in deep-inelastic positron-proton scattering at HERA. The distributions of jet polar angle, transverse energy, jet resolution, dijet mass, and other dijet variables are measured. Using parton densities derived from inclusive DIS cross sections, perturbative QCD calculations in NLO are found to give a consistent description of both the neutral and charged current dijet production. A direct, model independent comparison of the jet distributions in charged and neutral current events confirms that the QCD dynamics of the hadronic final state is independent of the underlying electroweak scattering process.

Abstract: 993, 994
Parallel session: 11,3
Plenary talk: 7 b,11

1 Introduction

Deep-inelastic scattering (DIS) at the electron-proton collider HERA offers unique possibilities to reveal the partonic structure of matter. At very high four-momentum transfer squared $-Q^2$ the exchange of all the electroweak gauge bosons (photon, Z^0 and $W^{\pm}$) becomes important allowing the standard model of electroweak and strong interactions to be tested at distances as small as 10^{-18}m. The inclusive DIS cross sections of neutral current (NC) $ep \rightarrow eX$ and charged current (CC) $ep \rightarrow \nu X$ interactions have been measured and are well described by the standard model [1]. In this analysis we complement these results by the first detailed measurement of the dijet structure of events in both NC and CC processes.

Within the Quark–Parton–Model, DIS gives rise to events with (1+1) jets where one jet originates from a quark struck out of the proton and a second jet is due to the proton remnant (denoted '+1'). Events with (2+1) jets, referred to as dijet events, are predicted by Quantum Chromodynamics (QCD) due to contributions in $O(\alpha_s)$, namely QCD–Compton scattering $eq \rightarrow eqg$ and Boson–Gluon–Fusion $eg \rightarrow eq\bar{q}$ as illustrated in Figure 1. Due to the relatively small number of CC events observed so far at HERA, the structure of the hadronic final state in CC interactions has not yet been studied in detail. Several CC events with multijet structures have been identified [2], and the jet shape in (single) jet CC events has been measured [3]. In NC interactions, clear multi-jet structures have been identified [4] and have been used to test QCD [5]. Previous analyses of dijet production in NC processes, however, did not yet extend to very high values of Q^2.

In the present paper a dijet analysis of a sample of ≈500 CC events and ≈8600 NC events with Q^2 in the range of 640 to 35 000 GeV^2 is performed. Various dijet distributions are compared with the predictions of QCD Monte Carlo models and with perturbative QCD calculations in next-to-leading order (NLO). Emphasis is placed on the region where both the virtuality of the exchanged boson Q^2 and the jet-jet invariant mass are as large as currently accessible. In addition, the jet distributions of the CC and the NC events are compared directly with each other, in order to test the expectation that QCD radiation is independent of the underlying electroweak scattering process.

2 Detector description and data selection

This analysis is based on the data sample recorded in the data taking periods 1994–1997 with the H1 detector at HERA. In this period HERA was operated with positron and proton beams of 27.5 and 820 GeV respectively, corresponding to a centre–of–mass energy of $\sqrt{s} = 300$ GeV. The collected integrated luminosity is 35.6 pb^{-1}.

2.1 Detector and trigger

The components of the H1 detector [6] most relevant for this analysis are the central tracking system, the liquid argon calorimeter and the instrumented iron return yoke.

The central tracking system consists of two concentric drift chambers covering a polar angular range[1] of 15° to 165°. Two polygonal drift chambers with wires perpendicular to the beam axis improve the determination of the z coordinate of the measured tracks. The central tracking system is surrounded by a liquid argon sampling calorimeter covering a polar angle range of $4° < \theta < 154°$. The electromagnetic and hadronic sections of the liquid argon calorimeter correspond in total to a depth of 4.5 to 8 interaction lengths. The energy resolution of the liquid argon calorimeter for electrons and hadrons was determined in test beam measurements to be $\sigma/E = 12\%/\sqrt{E(\mathrm{GeV})} \oplus 1\%$ and $\sigma/E = 50\%/\sqrt{E(\mathrm{GeV})} \oplus 2\%$, respectively [7]. The systematic uncertainty of the electromagnetic energy scale is determined to be 0.7% for the majority of the selected events [1] and increases to 3% at the highest Q^2. The uncertainty on the hadronic energy scale of the liquid argon calorimeter is 4%.

Outside the calorimeters a large superconducting solenoid provides a magnetic field of 1.15 Tesla. The instrumented iron return yoke identifies energetic muons and detects leakage of hadronic showers.

The trigger conditions for CC events are based on the reconstruction of a large missing transverse momentum in the trigger sums of the liquid argon calorimeter [8]. NC events are triggered on the basis of a high energy deposit in the electromagnetic part of the calorimeter [6].

2.2 Event selection

Selection of CC events

The selection of CC events is similar to those of [1, 9]. It is based on the observation of a large imbalance in transverse momentum in the detector due to the antineutrino escaping direct detection. The transverse momentum P_T^{had}, measured with the liquid argon calorimeter and the instrumented iron, is required to exceed 25 GeV. No scattered positron must be found thus excluding neutral current events. The z coordinate of the primary event vertex z_{vtx} has to be within a distance of ±35 cm from the nominal ep collision point. The inelasticity $y_{had} = \sum_h E_h(1 - \cos\theta_h)/2E_e$, calculated from the hadronic final state objects and the energy of the positron beam E_e, must be in the range $0.03 < y_{had} < 0.85$. The kinematic selection criteria imply a minimum virtuality Q^2 of the exchanged boson of 640 GeV^2.

Background events due to cosmic muons, beam-halo muons and beam-gas interactions are removed by further requirements on the event topology and timing [9]. Furthermore a visual scan of the remaining events is performed.

The final event sample consists of 460 CC events. The background from photoproduction events is less than 2%. It is estimated from Monte Carlo simulations and from data events where the scattered electron is detected at very small scattering angles. The number of background events from other sources is negligible.

The trigger efficiency for events with $P_T^{had} > 25$ GeV has been determined as a function of the kinematic variables and the jet variables studied using NC events discarding the information

[1] The forward direction and the positive z-axis are defined as the proton beam direction. The origin of coordinates is the nominal ep interaction point.

of the scattered positron [9]. The average trigger efficiency is $\approx 95\%$. It is corrected for in all measured distributions.

Selection of NC events
The kinematic selection criteria of the NC events correspond to those of the CC events. The NC selection requires the identification of the scattered positron. Fiducial cuts are applied to the impact position of the scattered positron in the liquid argon calorimeter in order to avoid inhomogeneities at the boundary of detector modules [1]. The kinematic selection is based on the variables P_T^e and y_e reconstructed from the scattered positron momentum with the exception of the requirement $y_{had} > 0.03$. The summed energy E and longitudinal momentum components P_Z of all reconstructed detector objects must fulfil $\sum E - Pz > 35$ GeV to suppress QED radiative events. The z coordinate of the primary event vertex is required to be in the same range as for the CC events. The NC sample consists of ≈ 8600 events with a negligible number of background events from photoproduction. The trigger efficiency of the NC events is $\approx 99\%$.

The distributions of the reconstructed kinematic variables P_T, Q^2, x and y for the CC and the NC event samples are shown in Figure 2. An excellent description of the data by the Monte Carlo model ARIADNE (see next section) combined with the H1 detector simulation is observed. Note that the distributions are normalized to the total number of CC or NC events N_{DIS} respectively. The differences between the CC and NC distributions are due to the different electroweak couplings and propagators relevant for CC and NC scattering.

The main selection criteria for the CC and NC events are summarized in Table 1.

CC	NC
no e^+ found	e^+ found
$P_T^{had} > 25$ GeV	$P_T^e > 25$ GeV
$0.03 < y_{had} < 0.85$	$0.03 < y_{had}, y_e < 0.85$
–	$E - P_Z > 35$ GeV
$\lvert z_{vtx}\rvert < 35$ cm	$\lvert z_{vtx}\rvert < 35$ cm

Table 1: Selection criteria for the CC and NC DIS event samples

3 QCD Monte Carlo models and QCD NLO programs

3.1 QCD Monte Carlo models

Four different QCD Monte Carlo models are used in this analysis: ARIADNE 4.10 [10]; HERWIG 5.9 [11], LEPTO 6.5.2β [12] and RAPGAP 2.08/06 [13]. All models use the LO matrix elements for QCD-Compton and Boson-Gluon-Fusion. ARIADNE implements higher order QCD radiation with radiating colour dipoles [14], HERWIG, LEPTO and RAPGAP use initial and final state parton showers instead [15]. In the context of this analysis LEPTO and RAPGAP are similar. They differ in the way the divergences of the LO matrix element are regulated. Fragmentation of partons into hadrons is modelled with the Lund string model [16] in ARIADNE, LEPTO and RAPGAP, and with the cluster model [17] in HERWIG.

The latest versions of the models as described in [18] are used. The LEPTO version used contains a refinement of soft-colour interactions, the generalised area law model [19]. LEPTO has been tuned to describe jet distributions at HERA and the corresponding values of the model parameters are taken here. In HERWIG, we use the leading order and not the next-to-leading order formula for α_s as proposed in [18]. The parton density functions CTEQ4L [20] are taken.

ARIADNE and LEPTO are incorporated into DJANGO [21], version 6.2, which simulates the effects of QED radiation.

3.2 QCD NLO programs

Four programs MEPJET [22], DISENT [23], DISASTER++ [24] and JETVIP [25] are available for perturbative QCD calculations of jet cross sections in NLO. Currently MEPJET is the only NLO program that considers W or Z^0 exchange. MEPJET is thus used to calculate the jet distributions in CC processes. The NC jet cross sections are calculated with DISENT following the recommendations in [27]. We use the parton density functions determined by the H1 collaboration [1] and choose Q^2 as the renormalization and factorization scales, μ_R^2 and μ_F^2.

We compared the predictions of MEPJET and DISENT for the jet distributions presented below. In leading order, we find agreement within a fraction of a per cent. In NLO, MEPJET is systematically lower than DISENT by $\approx 10\%$ confirming the results of [26]. Currently it is unknown if the inconsistencies between the NLO programs observed in NC influence the CC predictions as well.

DISENT does not consider Z^0 exchange which for $Q^2 > 5,000$ GeV^2 reduces the inclusive e^+p NC cross section by less than 5% on average compared with purely electromagnetic exchange. Since the dijet cross sections are also reduced, the effect on jet distributions normalized to the number of DIS events is small. Correction factors were calculated using ARIADNE 4.10 and are applied to any DISENT prediction at $Q^2 > 5000$ GeV^2.

In order to compare the perturbative QCD predictions to the data, bin-by-bin hadronization corrections are determined using the QCD models ARIADNE and HERWIG. The average correction factors from the two models are applied to the NLO distributions. The maximum deviation between the average correction factor and the correction factor for either model alone is taken as hadronization uncertainty.

4 Definition of jet observables

4.1 Jet algorithm

Jets are reconstructed with a modified version of the Durham jet algorithm which was originally introduced in e^+e^- annihilation. The algorithm is applied in the laboratory frame. It is modified for application in DIS in two respects: the scattered positron is removed from the final state objects; a missing-momentum four–vector is introduced which is treated as an additional object by the jet algorithm to account for the momentum carried by the proton remnant escaping through the beam pipe.

The jet algorithm calculates the quantity $k^2_{T,\,ij} = 2\min[E_i^2, E_j^2]\,(1 - \cos\theta_{ij})$ of pairs of objects or 'proto' jets i, j. Here E_i and E_j are the energies of the objects i and j, and θ_{ij} is the angle between them. The jet algorithm combines the pair of objects i, j with the minimum $k^2_{T,\,ij}$ to be a 'proto' jet by adding their four–momenta p_i and p_j. This prescription is repeated iteratively for the remaining objects until exactly (2+1) jets remain. At this stage, every event is treated as a dijet event by definition. Pronounced dijet structures are then selected by imposing a lower limit on y_2, defined as the minimum $k^2_{T,ij}/W^2$ of any combination of the (2+1) jets. Here, W is the invariant mass of the hadronic final state. It is calculated from all objects entering the jet algorithm.

In order to determine the fraction of events with (1+1) or (3+1) like jet structures it is more convenient to run the algorithm with a fixed jet resolution parameter y_{cut}. In this case the iterative clustering procedure ends, when the $k^2_{T,ij}/W^2$ of any pair of objects or proto jets is larger than a given value y_{cut}. Thus the number of jets reconstructed can be different for different events.

The algorithm is applied to the tracks reconstructed in the central tracking chambers and the energy depositions (clusters) in the liquid argon calorimeter. For tracks and calorimeter clusters that can be matched, double counting of the energy is avoided and the energy is determined from either the calorimeter alone or from a combination of track and cluster energy as described in [1]. The polar angle of each detector object, track or cluster, is required to exceed 7° in order to avoid the region close to the edge of the calorimeter. This improves the resolution of the reconstructed jet quantities.

The same definitions of the jets are used for the analysis of the data and the Monte Carlo events after detector simulation. In events simulated at the hadron or parton level and in the perturbative QCD calculations, the jet algorithm is applied to hadron or parton four-momenta respectively. The polar angle cut of 7°, which is applied for detector objects, is also applied for hadrons and partons.

The choice of a jet algorithm working in the laboratory frame leads to reduced experimental error since a boost into another frame is avoided. This is in particular relevant for the CC events where the resolution of the kinematic variables is worse than in NC events. The chosen reconstruction of W leads to a cancelation effect in y_2 and reduces the effect of the hadronic energy scale uncertainty on the measured jet distributions. In the following analysis the jet polar angles must fulfil $10 < \theta_{jet} < 140^\circ$. This restricts the jets to the acceptance of the liquid argon calorimeter.

4.2 Jet observables

The rate of events with different jet multiplicities is defined as $R_i(Q^2) \equiv N_i(Q^2)/N_{DIS}(Q^2)$, where $N_{i=1,2,3}$ is the number of events with one, two or three jets, respectively, besides the proton remnant jet. The value of y_{cut} is taken as 0.002.

The dijet sample is correspondingly defined by the requirement $y_2 > 0.002$. Large values of y_2 correspond to events with (2+1) jets that are clearly separated and indicative of hard QCD radiation. Small values of y_2 are typical for events which intuitively may be considered as (1+1) jet events. In Figure 3 two CC events with very different values of y_2 are displayed for illustration. Note that, with this definition of the dijet sample, the events contributing to the one-jet rate as introduced above are eliminated, and the few three-jet events are now treated as dijet events.

The distributions of the dijet variables y_2, m_{12}, z_p, x_p, the polar angle θ_{fwd} and the transverse energy $E_{T,fwd}$ of the most forward (non–remnant) jet are studied. m_{12} is the invariant mass of the two non-remnant jets. The variables z_p and x_p are defined by

$$z_p \equiv \min_{i=1,2}[E_i\,(1-\cos\theta_i)]/\sum_{i=1,2} E_i\,(1-\cos\theta_i) \quad \text{and} \quad x_p \equiv \frac{Q^2}{Q^2+m_{12}^2}$$

where E_i and θ_i are the energies and polar angles of the two (non–remnant) jets remaining after the clustering of the jet algorithm. For massless jets $z_p = 1/2 \min_{i=1,2}(1-\cos\theta_i^*)$ where θ^* is the scattering angle of the parton i in the centre-of-mass system of the virtual boson and the incoming parton. In leading order QCD x_p corresponds to the ratio x/ξ where ξ is the fraction of the proton's four momentum carried by the parton entering in the hard scattering process. In the limit where one jet is absorbed into the remnant jet z_p approaches 0. Correspondingly x_p approaches 1 if the two (non–remnant) jets become one jet.

5 Correction of the data

The data are corrected for the effects of detector acceptance and resolution, and of QED radiation using the QCD models ARIADNE and LEPTO. For the correction of CC events, the number of events simulated for either model is approximately 150 times larger than that of the experimental data. The number of simulated NC events is at least six times larger than that of the data. The same event cuts and track/cluster selection criteria are applied to the simulated events and to the data.

Correction of detector effects
The measured jet distributions are corrected for detector effects with bin-by-bin correction factors. The purity, defined as the fraction of reconstructed events where the value of the observable reconstructed from detector objects and that calculated from generated hadrons fall in the same bin, exceeds 50% in every bin of both CC and NC distributions. The purities estimated with LEPTO and ARIADNE are very similar.

The stability of the results was tested by correcting the jet distributions reconstructed from simulated LEPTO events with the correction factors derived with ARIADNE. The agreement of the corrected jet distributions with the 'true' LEPTO jet distributions calculated using the hadrons of the same events is good. Deviations are typically of a few percent. The largest deviations of $10-15\%$ are seen in the z_p distribution. These effects are considered in the model uncertainty discussed below.

Correction of QED radiative effects
The effects of QED radiation are considered by correction factors also. These factors are obtained from the ratio of the Monte Carlo distributions generated with and without inclusion of QED effects. The size of the corrections is $\approx 5\%$ for both CC and NC distributions.

The combined detector and QED radiation correction factors from LEPTO and ARIADNE are averaged, and the resulting mean correction factors are used to correct the jet distributions.

6 Determination of systematic errors

The three major sources of systematic errors are the model dependence of the detector corrections, the uncertainties of the electromagnetic and those of the hadronic energy scales of the liquid argon calorimeter. The total error of the majority of the CC data points is dominated by the statistical errors whereas the statistical and systematic errors are roughly of the same size for the NC data.

Model dependence of correction factors
The difference between the (average) corrected distributions and the distributions corrected with either model alone is taken as the error. The model dependence is on average $\approx 3\%$ for both the CC and NC distributions.

Electron energy calibration
The energy scale of electrons measured in the liquid argon calorimeter is known to 0.7% in the angular region where most events are situated. The effect on the jet distributions of the NC event sample is smaller than one per cent mostly.

Hadronic energy calibration
In order to estimate the effect of the hadronic energy scale uncertainty on the measured jet distributions, the analysis is repeated with the hadronic cluster energies shifted by $\pm 4\%$. The size of the corresponding changes depends considerably on the observable studied. For the CC events, the largest variation of $\approx 11\%$ is observed for the m_{12} distribution, the smallest variations of $\approx 3\%$ are observed for the y_2, z_p and θ_{fwd} distributions. Similar variations are observed in the NC jet distributions. A variation of the track momenta by $\pm 3\%$ has negligible effect on the jet distributions.

7 Results

7.1 Jet event rates

The rates of events with one, two and three jets $R_i(Q^2)$ are shown in Figure 4 as a function of Q^2. The jet rates for CC and NC events are similar. For the chosen jet resolution, the fraction of one-jet events is $\approx$ 70% for both CC or NC events. The fraction of dijet events is $\approx$ 20% and that of three-jet events is a few percent. For $Q^2 > 5000$ GeV^2 no CC three-jet events were measured. The Q^2 dependence of the jet rates is small. Note that R_1 has the weakest Q^2 dependence by definition since most of the DIS events are reconstructed as (1+1) jet events. The jet rates are well described by the QCD model ARIADNE.

7.2 Differential dijet distributions

The measured CC dijet distributions of y_2, m_{12}, z_p, x_p, $E_{T,\,fwd}$ and θ_{fwd}, corrected for detector and QED radiation, are shown in Figure 5. The measured differential dijet cross sections $d\sigma_{dijet}$ are normalized by the inclusive DIS cross section σ_{DIS} for the kinematic selection of section 2. The y_2 and m_{12} distribution are steeply falling. In the tails of these distributions events with clear dijet structures (see Figure 3) and with dijet masses up to $\approx$ 100 GeV are observed. The z_p distribution shows a drop in the first bin at small z_p which is due to the jet selection cut. The x_p distribution is strongly peaked at large values of x_p which is due to the dominance of events with relatively small m_{12} and due to the fact that Q^2 is large. This corresponding average value of ξ is $\approx$ 0.1 (as can also be estimated from the x distribution of Figure 2). The forward jet distributions are strongly increasing at small transverse energy and polar angles as is qualitatively expected by gluon bremsstrahlung off an incoming quark.

In Figure 6 the corresponding distributions are shown for NC events. They show the same features as the CC distributions. Note that the total error of the NC distributions is much smaller compared with that of the CC distributions.

The corrected jet distributions are compared with the QCD models ARIADNE, HERWIG, LEPTO and RAPGAP. Within the errors, the data are reasonably well described by the QCD models ARIADNE, HERWIG and RAPGAP. LEPTO roughly follows the data distributions but overall it is inferior to the other models. Significant deviations from the data are observed in the z_p distribution in particular. These observations are valid for both CC and NC distributions.

7.3 Comparison with perturbative QCD calculations in NLO

The differential dijet distributions are compared with QCD predictions in NLO. Two sources of theoretical error on the QCD predictions have been considered: the uncertainty of the hadronization corrections and the renormalization scale uncertainties. The size of these uncertainties is similar for CC and NC events. The hadronization corrections are typically smaller than 10%. The uncertainty of the hadronization corrections is estimated by the spread of the predictions of ARIADNE and HERWIG. The renormalization scale uncertainty of the NLO prediction is estimated by varying the renormalization scale μ_R^2 from Q^2 to 1/4 Q^2 and 4 Q^2. The resulting uncertainty is $\approx 5\%$. The mean transverse jet energy of any of the two non-remnant jets in the Breit frame $\langle E_T^{Breit} \rangle$ is ≈ 10 GeV. Choosing $\langle E_T^{Breit} \rangle^2$ as renormalization scale changes the NLO predictions by $\approx 5\%$ compared with the scale Q^2. A variation of the factorization scale has a marginal effect.

The CC jet distributions are compared with the NLO calculations of MEPJET in Figure 7. The MEPJET predictions provide a reasonable description of the data within errors. The corresponding NC distributions shown in Figure 8 are well described by the NLO predictions of DISENT.

In the Figures 7 and 8 the NLO predictions for quark- and gluon-induced processes are also shown separately [2]. The fraction of gluon-induced events is $\approx$ 20% in CC and $\approx$ 15% in NC

[2]Note that the normalizations σ_{DIS} of the quark-induced, gluon-induced and combined dijet cross sections are identical.

scattering for the cuts in this analysis. The dominance of quark-induced processes is mostly due to the relatively large values of x covered in this analysis. These fractions change by less than one per cent when varying the factorization scale in the QCD calculations from Q^2 to 1/4 and 4 Q^2. The existence of gluon-induced dijet processes in CC scattering has not yet been tested experimentally. Figure 7 shows that both quark and gluon contributions – calculated using the parton density functions determined from inclusive measurements – are needed to give a consistent description of dijet production in CC processes.

The CC and NC jet distributions have also been determined for the subsample of the selected DIS events with $Q^2 > 5000$ GeV^2. After the jet cuts 17 CC and 91 NC dijet events remain. In Figure 9 the corresponding dijet mass distributions are compared with the NLO predictions of MEPJET and DISENT. Agreement is found in all bins.

7.4 Direct comparison of CC and NC dijet distributions

In Figure 10 the jet distributions of the CC events (full circles) are compared with those of the NC events selected in the same kinematic range (lines). Systematic differences between the jet distributions are observed in several bins. This is expected due to the different electroweak couplings and gauge boson propagators which also lead to different kinematic distributions (see Figure 2). In order to remove these effects and to make possible a direct, model independent test of jet production in CC and NC processes, the NC events are reweighted to match the x and Q^2 spectra of the CC events. The weights are given by the ratio of the inclusive NC and CC DIS cross sections at the x and Q^2 of the NC event considered. The cross sections are calculated with DJANGO, considering QED radiative corrections. Note that the inclusive cross sections do not depend on the hadronic final state properties and thus the reweighting procedure is model independent.

The effect of this procedure has been tested with the QCD models ARIADNE and HERWIG, and the jet distributions of CC and reweighted NC events are predicted to agree within a few per cent typically. Residual differences between CC and reweighted NC jet distributions are expected due to the different fraction of gluon induced events in CC and NC processes, to helicity effects [31, 32], and to the different parton densities contributing to NC and CC scattering. The NC event selection was repeated with the cut $P_T^{had} > 25$ GeV instead of $P_T^e > 25$ GeV. The changes in the corrected jet distributions are of the order of 2%.

The measured NC jet distributions after reweighting are shown in Figure 10. Within errors they are found to be entirely consistent with the CC distributions.

8 Summary

A sample of 460 CC and of $\approx$ 8600 NC events produced in deep-inelastic e^+p scattering at HERA with the boson virtuality ranging from approximately $640 < Q^2 < 35,000$ GeV^2 have been selected. Jets are reconstructed using a modified version of the Durham algorithm. The analysis of the hadronic final state is extended to a kinematic region where only inclusive measurements have previously been made and where exchange of either gauge boson, photon, Z^0 and $W^{\pm}$ contributes.

Events with dijet structures are observed in CC processes. Differential CC dijet distributions are measured for the first time. Perturbative QCD calculations in NLO based on the MEPJET program describe the data well within errors. The measured distributions are sensitive to the presence of Boson-Gluon-Fusion processes in CC scattering. The NC dijet distributions, measured in the same kinematic range, are well described by perturbative QCD predictions in NLO based on DISENT.

The measured data sample contains events up to $Q^2 \approx 35\,000$ GeV^2 and $m_{12} \approx 100$ GeV and therefore provides a sensitive probe of the validity of the standard model at short distances. Using parton densities derived from NLO QCD fits to inclusive DIS cross sections, perturbative calculations based on the electroweak and the strong ($O(\alpha_s^2)$) matrix elements are found to give a consistent description of both the NC and CC jet cross sections at highest dijet masses and, simultaneously, highest Q^2.

A further test of jet production is performed comparing jet distributions of the CC events directly with those of the NC events. A simple reweighting method is presented which – to good approximation – removes the differences in the CC and NC jet distributions related to the different electroweak couplings and propagators in both processes. Comparison of the CC with the reweighted NC jet distributions confirms that the QCD dynamics of the hadronic final state is essentially independent of the underlying electroweak scattering process as is expected within the standard model.

References

[1] H1 Collaboration, C. Adloff *et al.*, DESY 99-107, submitted to Eur. Phys. J. **C**.

[2] ZEUS Collaboration, M. Derrick *et al.*, Z. Phys. **C72** (1996) 47.

[3] ZEUS Collaboration, J. Breitweg *et al.*, Eur. Phys. J. **C8/3** (1999) 367.

[4] H1 Collaboration, I. Abt *et al.*, Z. Phys. **C61** (1994) 59;
ZEUS Collaboration, M. Derrick *et al.*, Z. Phys. **C67** (1995) 81.

[5] see e.g. ZEUS Collaboration, M. Derrick *et al.*, Phys. Lett. **B363** (1995) 201;
H1 Collaboration, C. Adloff *et al.*, Eur. Phys. J. **C6** (1999) 4, 575;
H1 Collaboration, C. Adloff *et al.*, Eur. Phys. J. **C5** (1998) 4, 625;
H1 Collaboration, C. Adloff *et al.*, DESY 98-076, accepted by Eur. Phys. J. **C**.

[6] H1 Collaboration, I. Abt *et al.*, Nucl. Instr. and Meth. **A386** (1997) 310 and 348.

[7] H1 Calorimeter Group, B. Andrieu *et al.*, Nucl. Instr. and Meth. **A336** (1993) 499;
H1 Calorimeter Group, B. Andrieu *et al.*, Nucl. Instr. and Meth. **A350** (1994) 57.

[8] H1 Calorimeter Group, B. Andrieu *et al.*, Nucl. Instr. and Meth. **A336** (1993) 460.

[9] H1 Collaboration, S. Aid *et al.*, Phys.Lett. **B379** (1996) 319;
E. Chabert, Ph.D. thesis, University of Marseille, *in preparation*;
I. Negri, Ph.D. thesis, University of Marseille (1998).

[10] L. Lönnblad, Comp. Phys. Comm. **71** (1992) 15.

[11] G. Marchesini *et al.*, Comp. Phys. Comm. **67** (1992), 465.

[12] G. Ingelman, A. Edin and J. Rathsman, Comp. Phys. Comm. **101** (1997) 108.

[13] H. Jung, Comp. Phys. Comm. **86** (1995) 147;
RAPGAP program manual (1998) unpublished.

[14] G. Gustafson, Phys. Lett. **B175** (1986) 453;
G. Gustafson and U. Petterson, Nucl. Phys. **B306** (1988) 746;
B. Andersson, G. Gustafson L. Lönnblad and U. Petterson, Z. Phys. **C43** (1989) 625.

[15] M. Bengtsson and T. Sjöstrand, Comp. Phys. Comm. **37** (1988), 465.

[16] B. Andersson *et al.*, Phys. Rep. **97** (1983) 31;
T. Sjöstrand and M. Bengtssen, Comp. Phys. Comm. **43** (1987) 367.

[17] B.R. Webber, Nucl. Phys. **B238** (1984) 492.

[18] N.H. Brook, T. Carli, E. Rodriguez, M.R. Sutton, N. Tobien and M. Weber, Proceedings of the Workshop *Monte Carlo Generators for HERA Physics*, Eds. A.T. Doyle, G. Grindhammer, G. Ingelman and H. Jung, DESY-PROC-1999-02 10.

[19] J. Rathsman, Phys. Lett. **B452** (1999) 364.

[20] CTEQ Collaboration, H.L. Lai *et al.*, Phys. Rev. **D55** (1997) 1280.

[21] G.A. Schuler and H. Spiesberger, Proceedings of the Workshop *Physics at HERA*, Eds. W. Buchmüller and G. Ingelman, Vol. 3 (1991) 1419.

[22] E. Mirkes and D. Zeppenfeld, Phys. Lett. **B380** (1996) 205.

[23] S. Catani and M.H. Seymour, Nucl. Phys. **B485** (1997) 291.

[24] D. Graudenz, hep-ph/9710244.

[25] B. Pötter, Comp. Phys. Comm. **119** (1999) 45.

[26] C. Duprel, Th. Hadig, N. Kauer and M. Wobisch, Proceedings of the Workshop *Monte Carlo Generators for HERA Physics*, Eds. A.T. Doyle, G. Grindhammer, G. Ingelman and H. Jung, DESY-PROC-1999-02 142;
G. McCance, ibid. 151.

[27] D. Graudenz and M. Weber, Proceedings of the Workshop *Monte Carlo Generators for HERA Physics*, Eds. A.T. Doyle, G. Grindhammer, G. Ingelman and H. Jung, DESY-PROC-1999-02 117.

[28] JADE Collaboration, W. Bartel *et al.*, Z. Phys. **C33** (1986) 23;
JADE Collaboration, S. Bethke *et al.*, Phys. Lett. **B213** (1988) 235.

[29] T. Brodkorb, J.G. Körner, E. Mirkes, G.A. Schuler, Z. Phys. **C44** (1989) 415;
D. Graudenz, N. Magnussen, Proceedings of the Workshop *Physics at HERA*, Eds. W. Buchmüller and G. Ingelman, DESY (1991) 261.

[30] S. Catani *et al.*, Phys. Lett. **B269** (1991) 432.

[31] J.G. Körner, E. Mirkes and G.A. Schuler, Int. J. Mod. Phys. **A4** (1989) 1781;
E. Mirkes, TTP-97-39, University of Karlsruhe and hep-ph/9711224.

[32] M. H. Seymour, Nucl. Phys. **B436** (1995) 443.

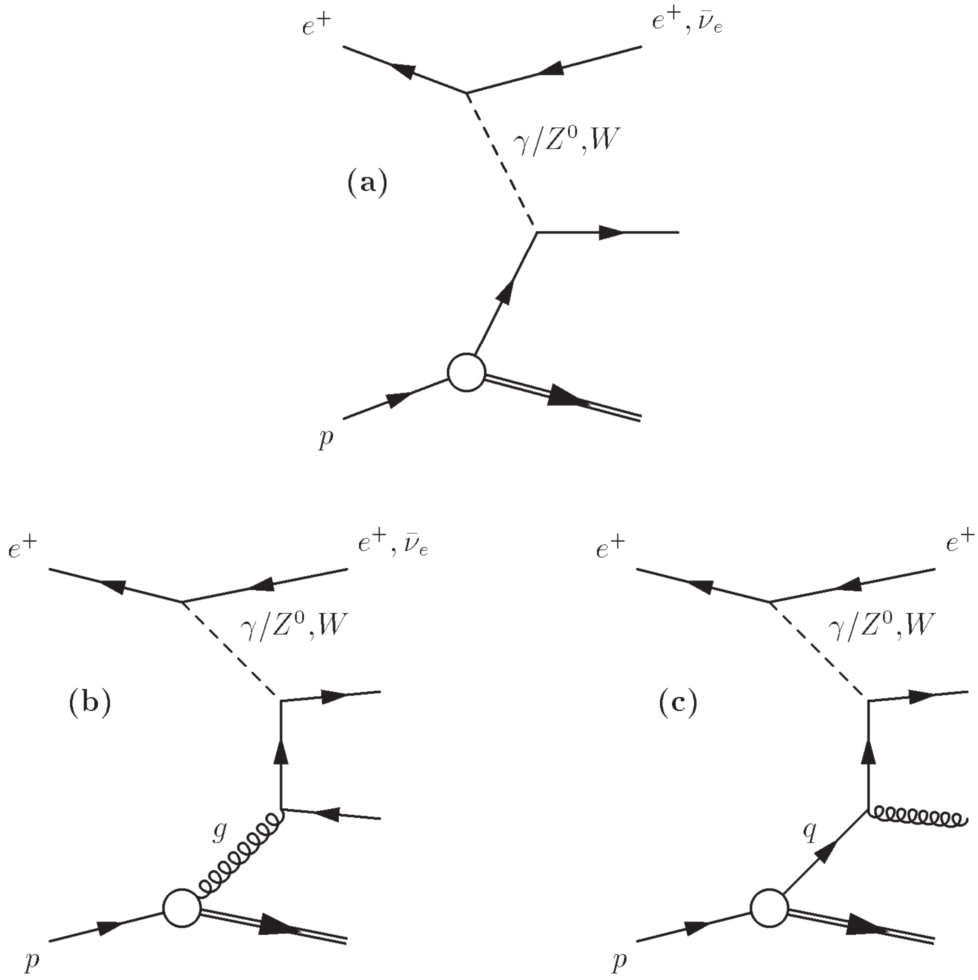

Figure 1: Feynman graphs for DIS in lowest order (a), and selected leading-order diagrams contributing to dijet production: Boson–Gluon–Fusion (b) and QCD–Compton scattering (c).

H1 preliminary

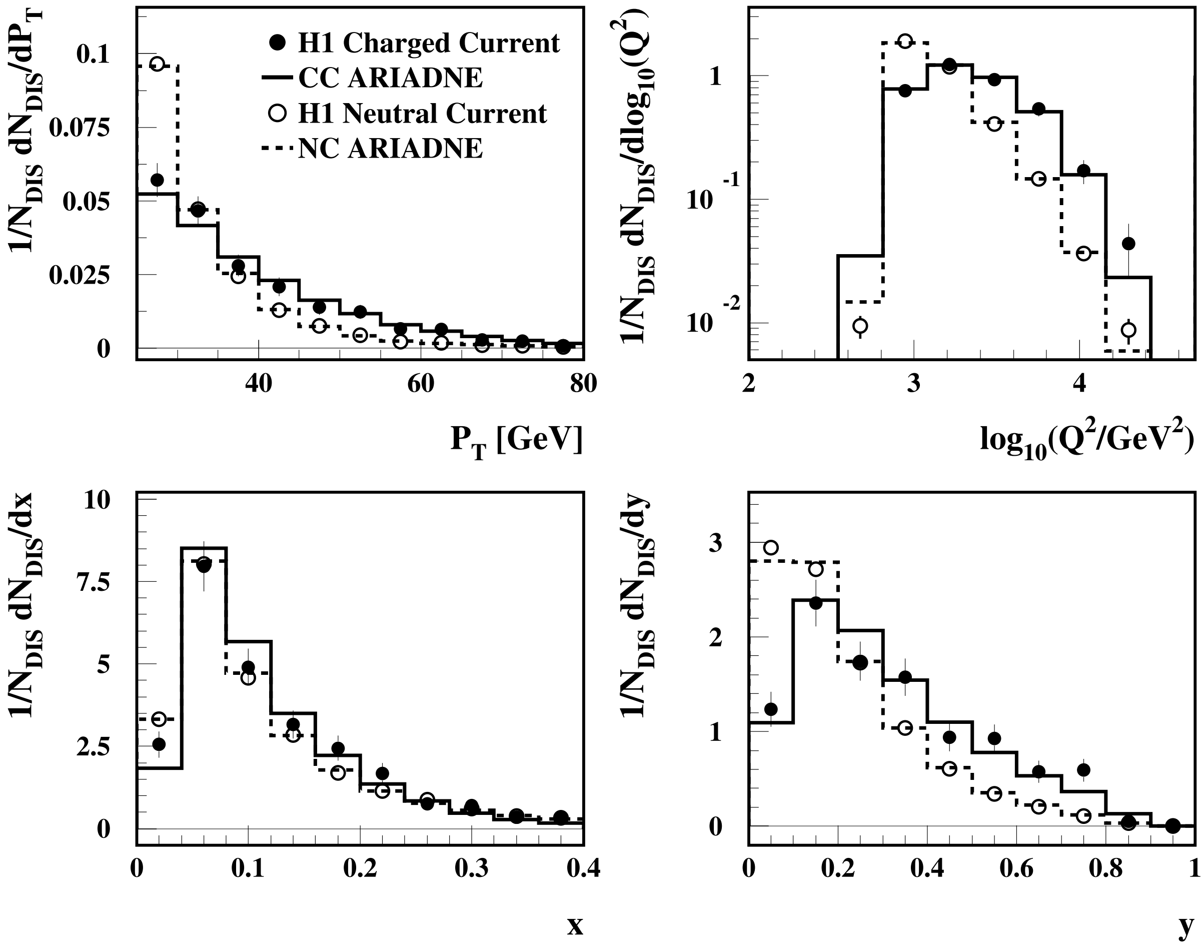

Figure 2: Uncorrected data distributions of P_T, Q^2, x and y for the selected CC and NC events. The observables are calculated using the hadronic final state for CC events, and the scattered positron for NC events. The errors are statistical only. Also shown are the corresponding predictions of the MC model ARIADNE 4.10 including radiative QED corrections and the H1 detector simulation for CC processes (full line) and NC processes (dashed).

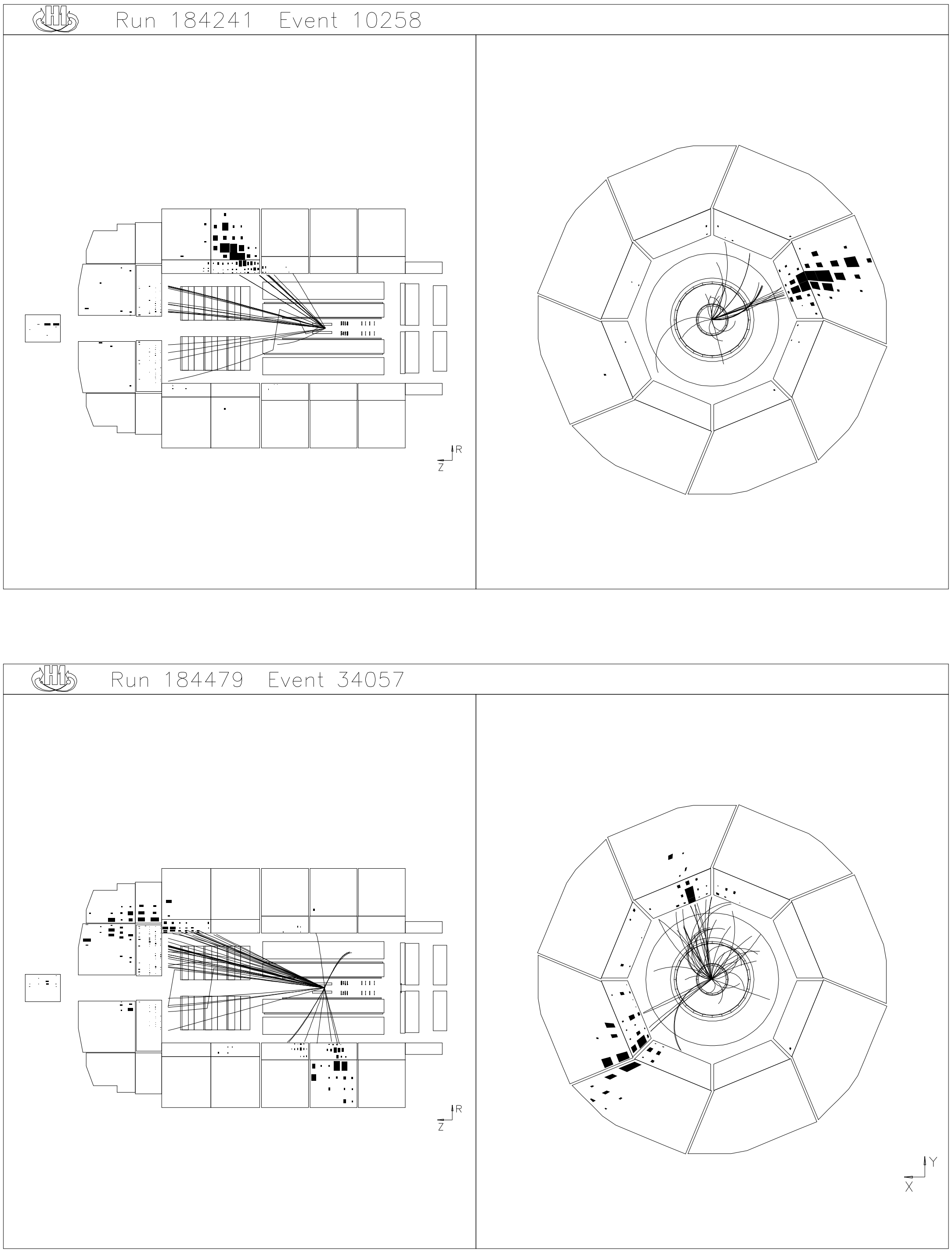

Figure 3: A display of two CC events. The left part shows a side view of the H1 central and forward tracking systems surrounded by the electromagnetic and hadronic sections of the liquid argon calorimeter and of the lead/scintillating-fibre calorimeter. The full lines and filled rectangles correspond to tracks reconstructed in the tracking systems and energy depositions in the calorimeter, respectively. The proton beam enters from the right. The right part shows a view along the beam of the same events. For the upper event $y_2 \approx 0.00008$ and $m_{12} \approx 12$ GeV. For the the lower event $y_2 \approx 0.01$ and $m_{12} \approx 83$ GeV.

H1 preliminary

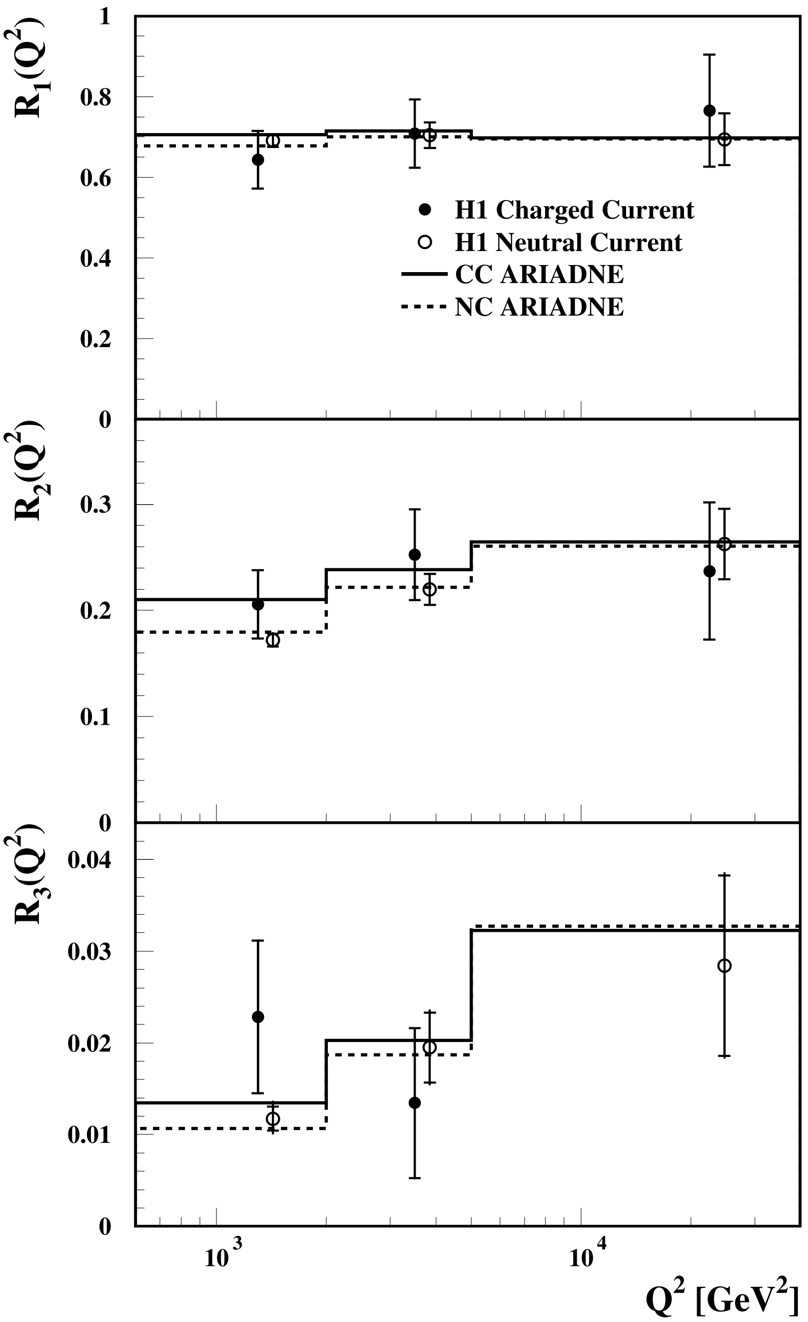

Figure 4: CC and NC event rates with one, two and three jets as a function of Q^2. The events satisfy $P_T^{lept} > 25$ GeV and $0.03 < y < 0.85$. The jets are reconstructed using the modified Durham algorithm with a fixed jet resolution parameter $y_{cut} = 0.002$. The jets satisfy the cut $10 < \theta_{jet} < 140°$. The distributions are corrected for detector effects and the effects of QED radiation. The inner and outer error bars represent the statistical and total errors, respectively. Also shown are the predictions of the MC model ARIADNE 4.10.

H1 preliminary

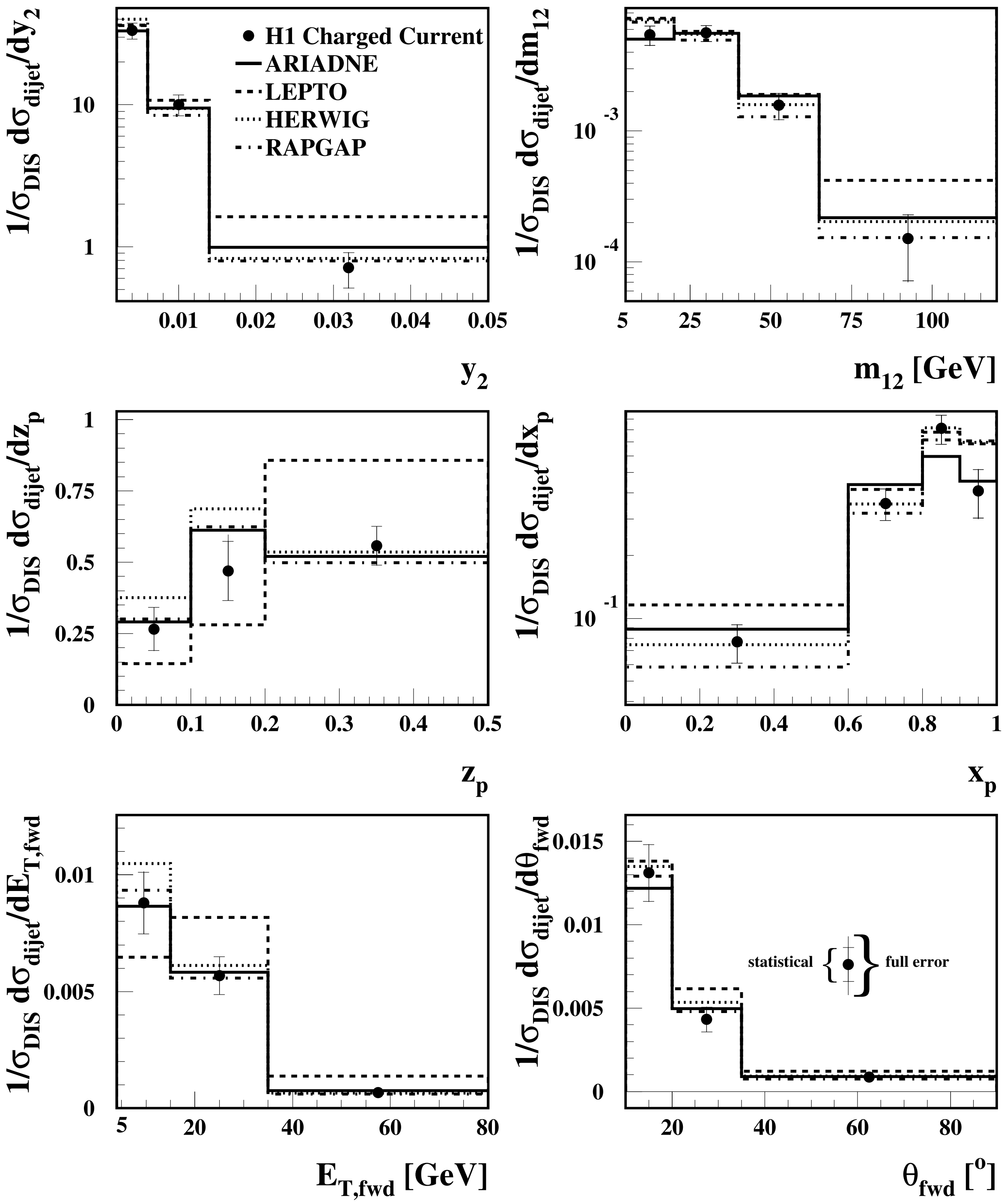

Figure 5: Distributions of y_2, m_{12}, z_p, x_p, $E_{T,\,fwd}$ and θ_{fwd} in CC events with $P_T^{lept} > 25$ GeV and $0.03 < y < 0.85$ determined with the modified Durham algorithm. The events satisfy the cuts $y_2 > 0.002$ and $10 < \theta_{jet} < 140°$. The distributions are corrected for detector effects and the effects of QED radiation. The inner and outer error bars represent the statistical and total errors, respectively. Also shown are the predictions of the MC models ARIADNE 4.10 (full line), LEPTO 6.5.2β (dashed), HERWIG 5.9 (dotted) and RAPGAP 2.08/06 (dashed-dotted).

H1 preliminary

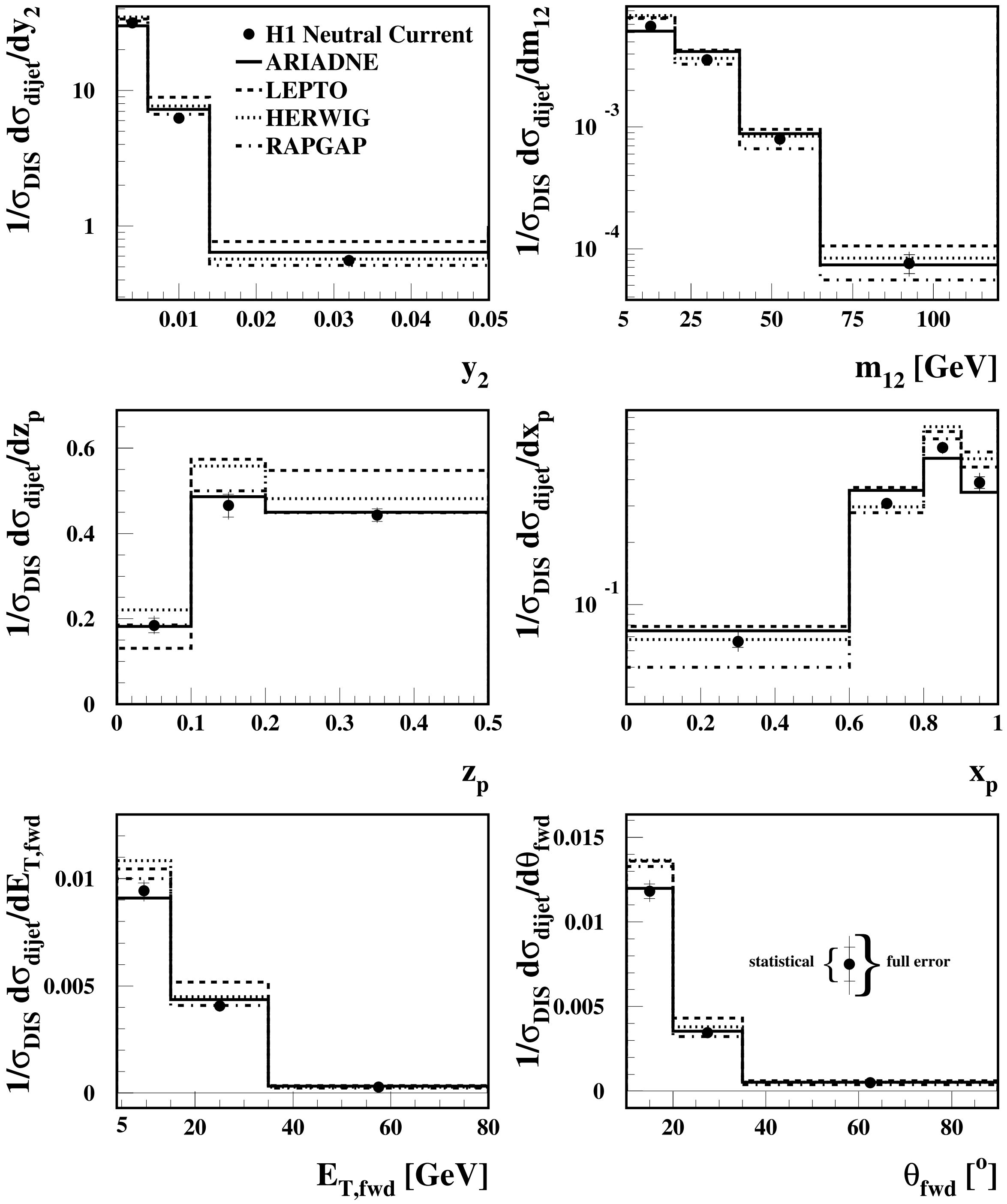

Figure 6: Distributions of y_2, m_{12}, z_p, x_p, $E_{T,\,fwd}$ and θ_{fwd} in NC events with $P_T^{lept} > 25$ GeV and $0.03 < y < 0.85$ determined with the modified Durham algorithm. The events satisfy the cuts $y_2 > 0.002$ and $10 < \theta_{jet} < 140°$. The distributions are corrected for detector effects and the effects of QED radiation. The inner and outer error bars represent the statistical and total errors, respectively. Also shown are the predictions of the MC models ARIADNE 4.10 (full line), LEPTO 6.5.2β (dashed), HERWIG 5.9 (dotted) and RAPGAP 2.08/06 (dashed-dotted).

H1 preliminary

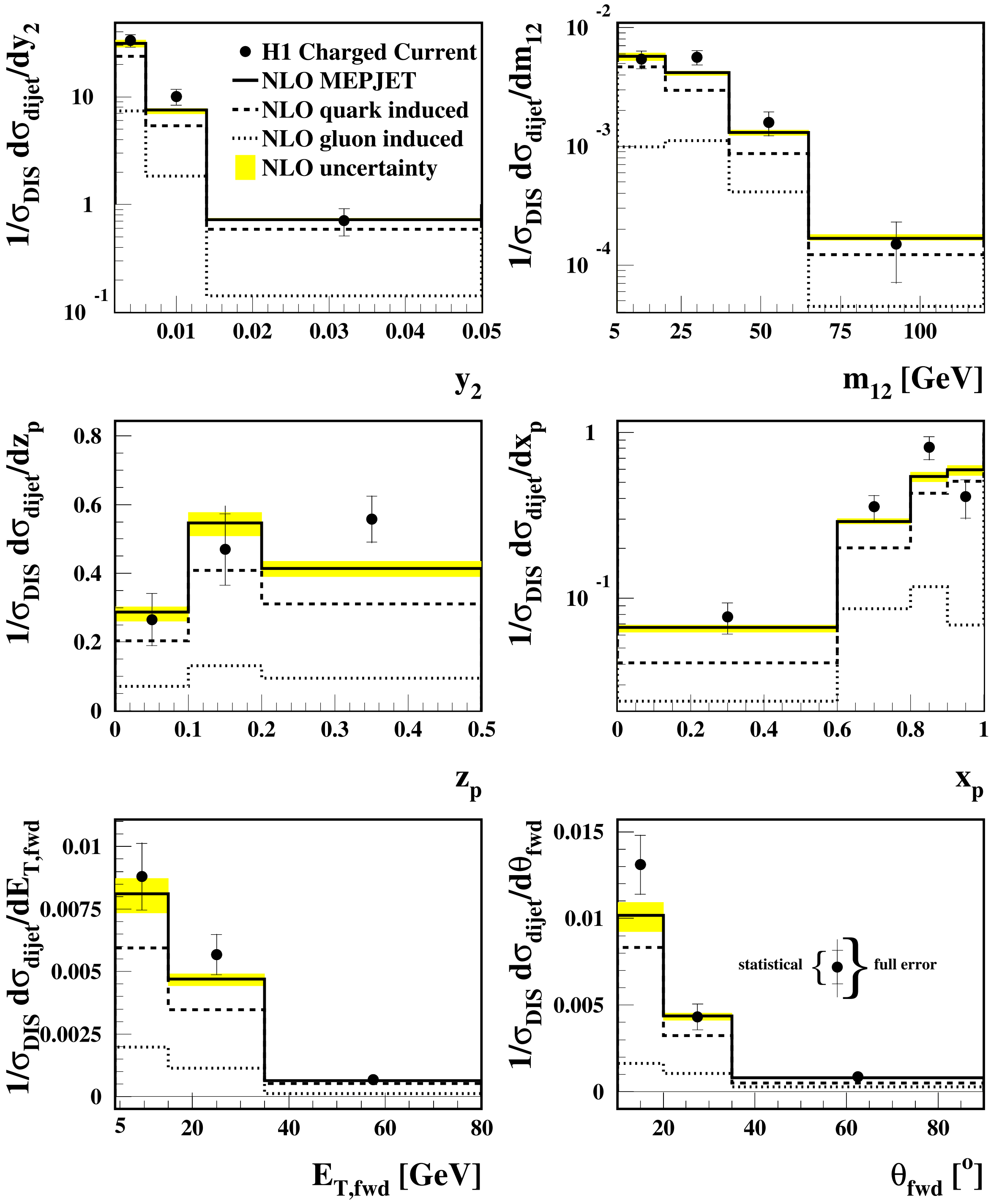

Figure 7: Distributions of y_2, m_{12}, z_p, x_p, $E_{T,\,fwd}$ and θ_{fwd} in CC events with $P_T^{lept} > 25$ GeV and $0.03 < y < 0.85$ determined with the modified Durham algorithm. The events satisfy the cuts $y_2 > 0.002$ and $\theta_{jet} < 140°$. The distributions are corrected for detector effects and the effects of QED radiation. The inner and outer error bars represent the statistical and total errors, respectively. Also shown are perturbative QCD calculations in NLO obtained with MEPJET combined with a correction for hadronization effects. The shaded area shows the hadronization uncertainties and the renormalization scale uncertainties of the NLO calculations added in quadrature. In addition, the jet distributions obtained for quark- and gluon-induced processes are shown separately.

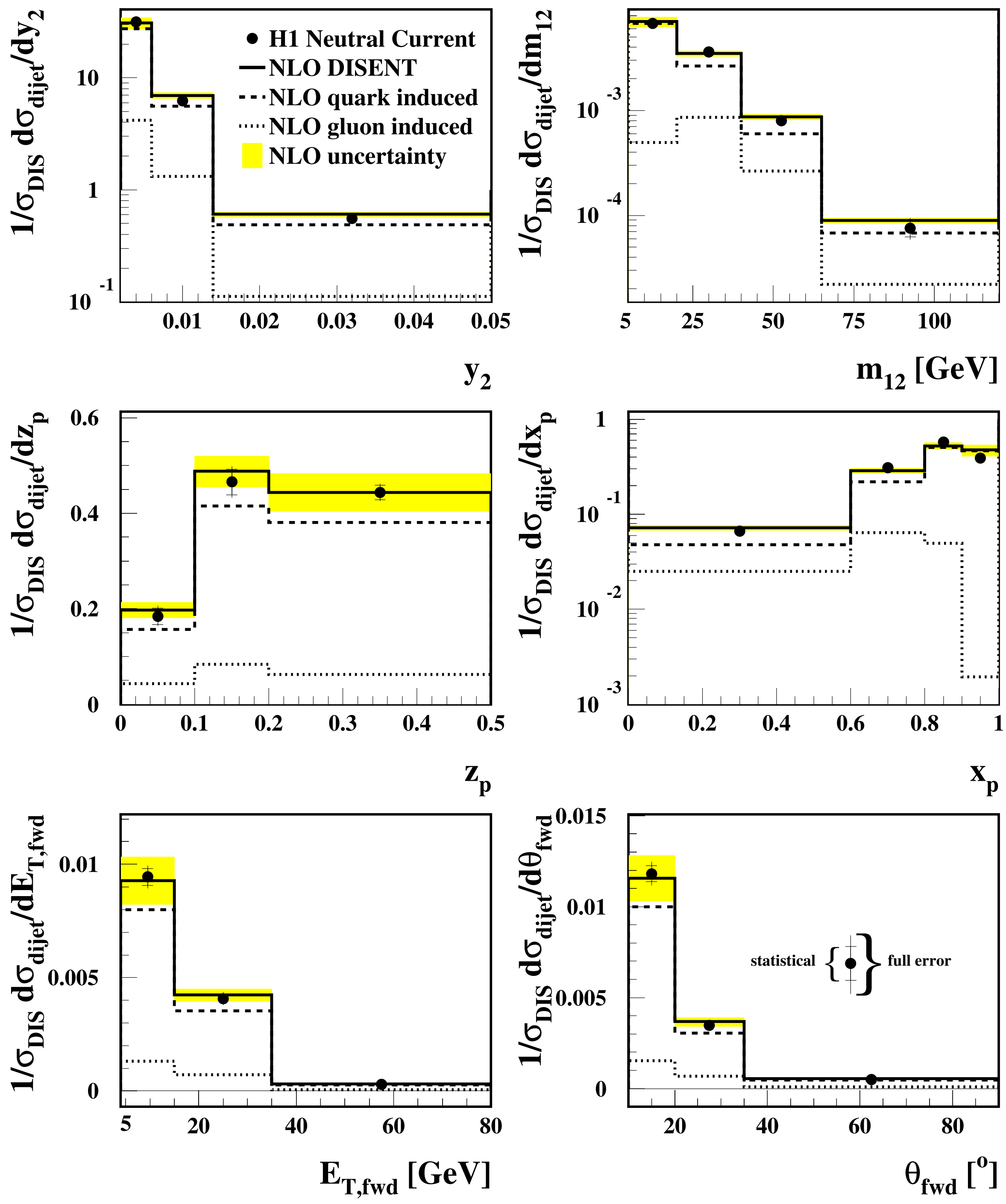

Figure 8: Distributions of y_2, m_{12}, z_p, x_p, $E_{T,\,fwd}$ and θ_{fwd} in NC events with $P_T^{lept} > 25$ GeV and $0.03 < y < 0.85$ determined with the modified Durham algorithm. The events satisfy the cuts $y_2 > 0.002$ and $10 < \theta_{jet} < 140°$. The distributions are corrected for detector effects and the effects of QED radiation. The inner and outer error bars represent the statistical and total errors, respectively. Also shown are perturbative QCD calculations in NLO obtained with DISENT combined with a correction for hadronization effects. The shaded area shows the hadronization uncertainties and the renormalization scale uncertainties of the NLO calculations added in quadrature. In addition, the jet distributions obtained for quark- and gluon-induced processes are shown separately.

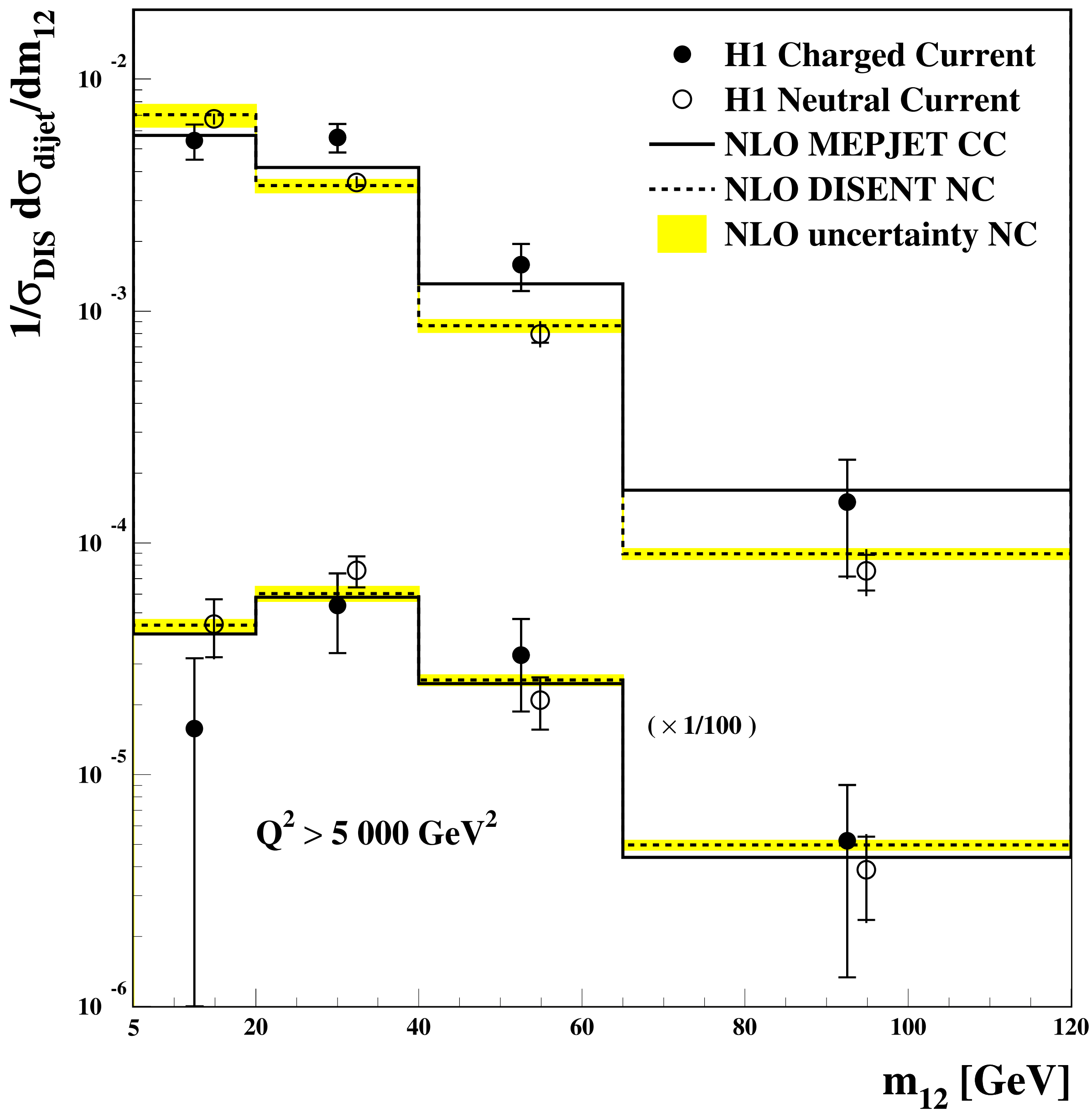

Figure 9: Distributions of m_{12} in CC events (full circles) and NC events (empty circles) for $P_T^{lept} > 25$ GeV and $0.03 < y < 0.85$ with and without the additional requirement $Q^2 > 5000$ GeV determined with the modified Durham algorithm. The events satisfy the cuts $y_2 > 0.002$ and $10 < \theta_{jet} < 140°$. The distributions are corrected for detector effects and the effects of QED radiation. The inner and outer error bars represent the statistical and total errors, respectively. Also shown are perturbative QCD calculations in NLO obtained with MEPJET (for CC) and DISENT (for NC) combined with a correction for hadronization effects. The lower histograms and the corresponding data points have been scaled by a factor of 1/100. The shaded area shows the hadronization uncertainties and the renormalization uncertainties of the NLO calculations added in quadrature. For clarity, the NC uncertainties are shown only. The CC uncertainties are of similar size.

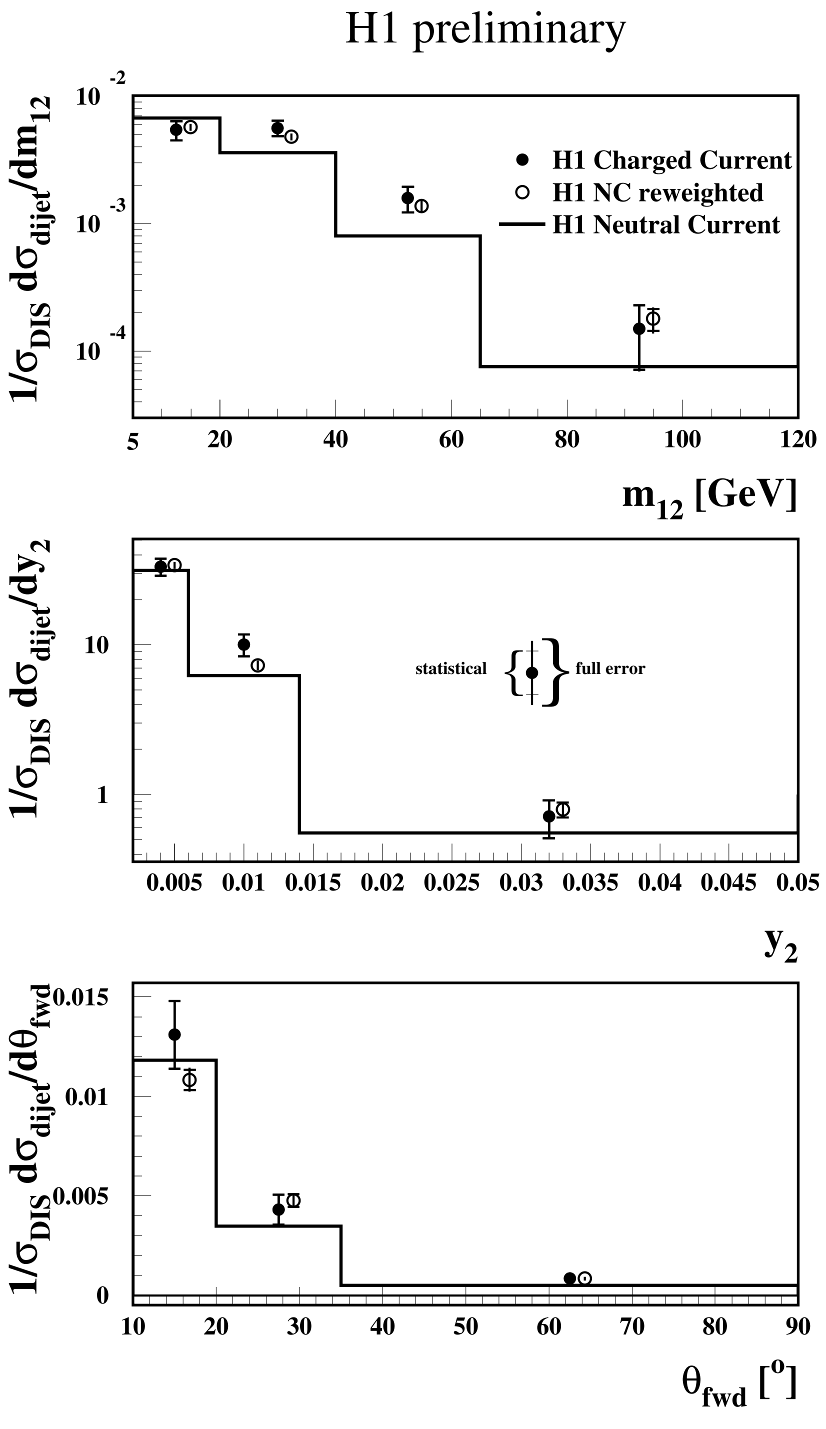

Figure 10: The distributions of m_{12}, y_2 and θ_{fwd} in CC events (full circles) and the corresponding distribution in NC events with (empty circles) and without reweighting (lines) as described in the text. The same jet selection criteria as above are applied. The distributions are corrected for detector effects and the effects of QED radiation. The inner and outer error bars represent the statistical and total errors, respectively. The errors of the reweighted NC distribution are not shown. They are of the same size as those of the unreweighted NC distributions.